Optimizing Interface Conductivity in Electronics

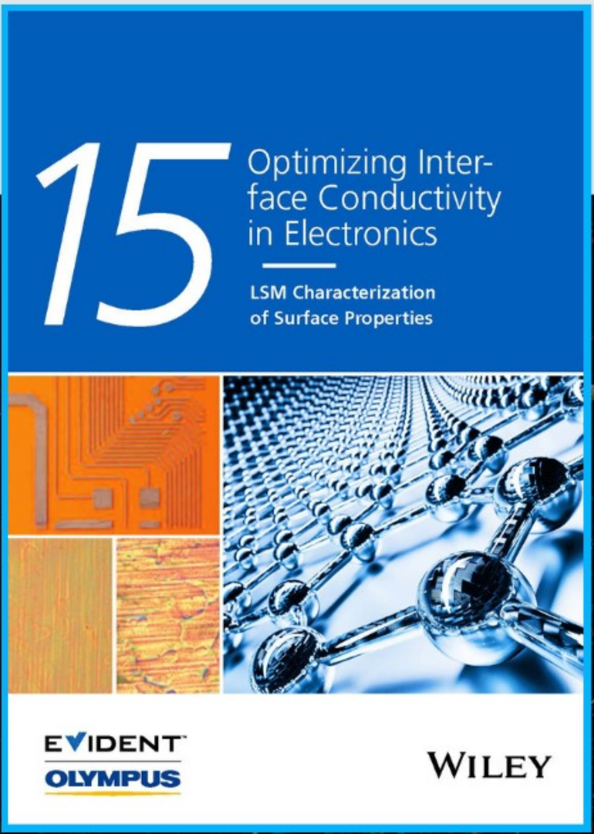

15

Optimizing Interface Conductivity in Electronics

LSM Characterization of Surface Properties

EVIDENT

OLYMPUS

WILEY

The latest eBook from Advanced Optical Metrology. Download for free.

Surface roughness is a key parameter for judging the performance of a given material's surface quality for its electronic application. A powerful tool to measure surface roughness is 3D laser scanning confocal microscopy (LSM), which will allow you to assess roughness and compare production and finishing methods, and improve these methods based on mathematical models.

Focus on creating high-conductivity electronic devices with minimal power loss using laser scanning microscopy is an effective tool to discern a variety of roughness parameters.

EVIDENT

OLYMPUS

WILEY

RESEARCH ARTICLE

ADVANCED FUNCTIONAL MATERIALS
www.afm-journal.de

Dynamic Concentration of Alloying Element on Anode Surface Enabling Cycle-Stable Li Metal Batteries

*Xiancheng Wang, Yufang He, Shiyu Liu, Yuanjian Li, Shuibin Tu, Renming Zhan, Zihe Chen, Junjie Fu, Zhao Cai, Li Wang, and Yongming Sun**

The pursuit of high energy density Li-based rechargeable batteries has intrigued numerous research interest on Li metal anode. However, several significant challenges, including severe parasitic reactions and growth of Li dendrites, lead to fast electrode failure and impede its practical implantation. Herein, it is revealed that the dynamic concentration of alloying element in Li solid solution can significantly improve the cycling stability. It is demonstrated that the alloying element of Li solid solution continuously evolved in the reaction layer on cycling. Alloying element got enriched on anode surface after Li stripping, and re-dispersed into the deposited Li during Li plating processes. The alloying element-rich surface can reduce the Li nucleation barrier and promote the uniform Li plating behavior. Ultrathin Li solid solution foils are fabricated, and the dynamic alloying element concentration mechanism is further verified, and the cycling lifespan of pure Li is doubled. Consequently, a 1.4 Ah laminated pouch cell with ultrathin Li solid solution anode (30 µm) exhibits high energy density of 836 Wh L^{-1} and stable cycling performance under the harsh conditions with low negative/positive capacity (N/P) ratio of 2 and electrolyte/capacity (E/C) ratio of 2.6 g Ah^{-1}.

1. Introduction

The development of battery chemistry beyond the state-of-the-art Li-ion intercalation mechanism provides great opportunities for achieving higher energy density than the existing energy storage systems.[1–3] Li metal anode exhibits the high specific capacity (3860 mAh g^{-1}) and the lowest electrode potential (−3.04 V vs standard hydrogen electrode) among all the anode candidates of Li-based rechargeable batteries, and receives great research attention in the past years.[4–6] However, metallic Li possesses intrinsic high chemical reactivity and relatively infinite volume change, which cause the continuous parasitic reactions between active Li and electrolyte, leading to fast electrochemical performance degradation.[7–9] Besides, metallic Li dendrites would be produced during the electrochemical plating processes due to the high Li nucleation barrier and the slow Li ion diffusion at the electrode/electrolyte interface, giving rise to the safety concerns of rechargeable Li metal batteries.[10,11]

Till now, numerous studies have been conducted to address the above-mentioned issues of metallic Li anode and improve its electrochemical performance. Electrolyte component regulation (e.g., using fluoride, nitride, and oxide additives)[12–14] and electrode interface engineering (e.g., construction of liquid alloy interphase, alloy/fluoride hybrid interphase, and salt-philic/solvent-phobic polymer layer)[15–17] could enable a stable and robust shield for metallic Li against corrosive electrolyte, and thus suppress parasitic reaction and prolong the cycling life of Li metal anode. Besides, dendritic Li depositions could be alleviated due to the homogenized charge transfer at the electrode interface.[18,19] Host design for Li metal could provide a mechanical support and buffer the volume change, and thus restrain the anode pulverization during Li stripping/plating processes.[20,21] The lithiophilic property of a host could further improve the homogeneity for Li plating and enhance the cycling stability of Li metal anode.[22,23] Specifically, the bonus of fast charge transfer could be achieved for Li metal composite with a Li$^+$ conductive alloy host.[24,25] Despite of these great research achievements, the electrochemical performance of the state-of-the-art Li metal anode still cannot satisfy the demand for practical rechargeable Li metal batteries. Advanced material/electrode designs based on novel mechanism are highly desirable for realizing stable Li metal anode with high Li utilization and long cycle lifespan for practical harsh application conditions.

X. Wang, S. Liu, S. Tu, R. Zhan, Z. Chen, J. Fu, Y. Sun
Wuhan National Laboratory for Optoelectronics
Huazhong University of Science and Technology
Wuhan 430074, China
E-mail: yongmingsun@hust.edu.cn

Y. He, L. Wang
Institute of Nuclear and New Energy Technology
Tsinghua University
Beijing 100084, China

Y. Li
Institute of Materials Research and Engineering (IMRE)
Agency for Science
Technology and Research (A*STAR)
2 Fusionopolis Way, Innovis #08-03, Singapore 138634, Singapore

Z. Cai
Faculty of Materials Science and Chemistry
China University of Geosciences (Wuhan)
Wuhan 430074, China

The ORCID identification number(s) for the author(s) of this article can be found under https://doi.org/10.1002/adfm.202307281

DOI: 10.1002/adfm.202307281

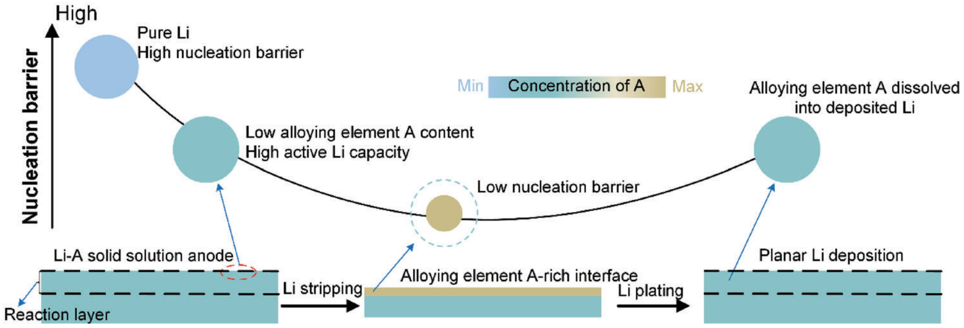

Figure 1. Schematic of dynamical concentration of alloying element at electrode interphase during Li stripping/plating processes.

Li intermetallic compound with good Li affinity and high Li ion diffusion coefficient could reduce the Li nucleation barrier, facilitate surficial Li migration, and hinder the Li dendrite formation, enabling superior electrochemical cycling stability of Li/Li intermetallic compound composite anodes (e.g., Li/$Li_{22}Sn_5$, Li/Li_xIn and Li/ZnF_2).[26–28] However, there exists the trade-off between the high content requirement of Li intermetallic compound and the regulation effect of Li plating/stripping behavior. A high mass ratio of Li intermetallic compound is often demanded to construct an effective interface for regulating Li plating processes,[29,30] which leads to low overall Li specific capacity of hybrid anode and significantly reduces the energy density of the batteries.[31,32] In principle, dynamic evolution of alloying element content on the surface of Li composite anode is ideal for balancing active Li capacity and cycle life. Alloying element gets enriched on the surface of composite anode during the Li stripping processes, and such the formed interface layer could regulate the subsequent Li plating processes. Thus, high specific capacity, dendrite-free Li plating, and good cycling stability with high Li utilization could be synchronously achieved for Li metal anode by such a mechanism of dynamical concentration of alloying element at anode surface.

In this study, we investigated the component evolution of Li solid solution anode during electrochemical Li stripping/plating cycling, as well as its special effect on improving the electrochemical performance. The introduction of Ag and Mg spices would help the formation of the signal-phase Li solid solution (Figure S1, Supporting Information).[33,34] Li extraction takes place from the solid-solution electrochemical reaction layer during Li stripping processes, which enables the dynamic concentration of alloying element on the anode surface.[35,36] The high concentration of alloying element on electrode surface thus reduces the Li nucleation barrier, and regulates the subsequent Li plating processes. It is worth noted that such a dynamic regulation mechanism for electrochemical Li stripping/plating behavior significantly differs from that for Li intermetallic compound-based composites, for which the component and structure of Li intermetallic compound remain constant during cycling.[37,38] To reveal the great merits of such a novel mechanism, ultrathin Li solid solution (Li-Ag and Li-Mg) anodes with high active Li capacity of ≈3400 mAh g^{-1} were explored (Figure S3, Supporting Information), and they showed doubled cycle lifespan in comparison to pure Li metal anode in both symmetric and full cell configurations under the same test condition. The assembled 1.4 Ah laminated $LiNi_{0.6}Co_{0.2}Mn_{0.2}O_2$ (NCM622)||Li-Ag (30 µm in thickness) pouch cell displayed a high energy density of 836 Wh L^{-1}, as well as stable cycling performance under harsh conditions with a low N/P ratio of 2 and E/C ratio of 2.6 g Ah^{-1}.

2. Results and Discussions

2.1. Mechanism of the Dynamic Concentration of Alloying Element at Anode Interface

Figure 1 schematically illustrated the component evolutions of the Li-A (A represents alloying element, Ag or Mg in this work) solid solution anode during the Li stripping/plating processes. Alloying element A gradually gets enriched accompanied by the electrochemical Li extraction on the electrode surface during Li stripping process. Afterward, such an alloying element A-rich electrode surface would reduce the Li nucleation barrier and help to achieve planar Li deposition during the subsequent Li plating process.[39,40] In the inverse process, alloying element A would be dissolved into the deposited Li, leading to the effect regulation for continuous Li deposition. Such mechanism of dynamical concentration of alloying element on electrode surface could enable the dendrite-free, stable electrochemical cycling performance of Li solid solution anodes.

To verify the dynamic concentration of alloying element on anode surface, we conducted back-scattered electron (BSE) images with element mappings by electron probe microanalysis (EPMA) for the Li-Ag solid solution anode under different Li stripping/plating states. The results demonstrated the increased intensity of Ag element signal after Li stripping (5 mAh cm^{-2}) and the decreased intensity of Ag element signal after subsequent Li plating (3 mAh cm^{-2}) (**Figure 2**a–c), revealing that an alloying element Ag-rich interface dynamically formed during the Li stripping/plating processes. Also, the Ag element would be dispersed into as-deposited Li metal, regulating the subsequent Li plating processes. A similar phenomenon could be observed on the Li-Mg solid solution anode (Figure S4, Supporting Information), indicating the universality of dynamical concentration of alloying element on the electrode surface in Li solid solution anodes. Auger electron spectroscopy (AES) was further employed to probe the dynamic content change of Ag element on the electrode surface under different Li stripping/plating states. As shown in Figure 2d, the highest intensity of Ag peak was shown at the Li stripping state of the Li-Ag foil, which became weaker after Li plating (the corresponding kinetic energies of Li and Ag were shown in Table S1, Supporting Information). The atomic ratios of

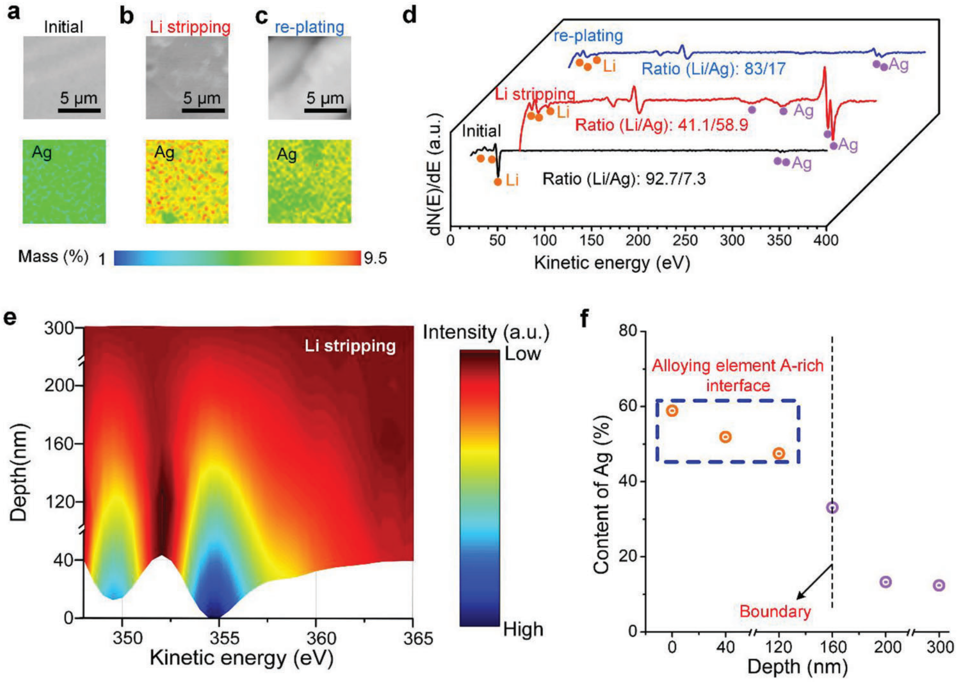

Figure 2. BSE images of Li-Ag solid solution anode and the corresponding Ag element mapping images a) at the initial state, b) after Li stripping (5 mAh cm^{-2}), and c) after Li re-plating (3 mAh cm^{-2} Li) detected by EPMA. d) AES spectra of Li-Ag foil electrode at different Li stripping/plating states. e) AES spectra for Li-Ag solid solution anode after Li stripping (5 mAh cm^{-2}) with different Ar^{+} etching depth and f) the corresponding Ag atomic content-depth plot (The atomic content was calculated by the ratio of Ag/(Li+Ag)). The etching depth was referred with the standard sample of SiO$_2$ for different etching time.

Li/Ag for the initial Li-Ag foil, and the foils after Li stripping and re-Li plating were evaluated to be 92.7:7.3, 41.1:58.9, and 83:17, respectively, which again supported the dynamic concentration of Ag element on electrode surface. We further examined the Ag content change along the depth of the Li-Ag anode using AES. The signal intensity gradually got weaker with the increase of etching depth (Figure 2e, Figure S5, Supporting Information). The measured value of Ag atomic content was around 50 at% from the etching depth from 0 to 120 nm, and it decreased to 30 at% at 160 nm, and then to 10 at% at 200 nm (Figure 2f). It remained constant when further increasing the etching depth, which is close to the value for the pristine Li-Ag foil. These results verified that a thin Ag-rich surface layer was formed on the electrode surface during the electrochemical Li plating process. High Ag content at Li stripping state could help to reduce Li nucleation barrier and facilitate Li diffusion on electrode surface, thus enable planar electrochemical Li plating behavior and prolong cycling lifespan.[41,42]

2.2. The Electrochemical Performance and Characterization of Li Solid Solution Anode

We further evaluated the electrochemical performance of the Li solid solution anodes. **Figure 3**a shows the voltage-time plots for the Li||Li, Li-Mg||Li-Mg (10 wt% Mg), and Li-Ag||Li-Ag (10 wt% Ag) cells with controlled thin electrode thickness of 50 µm in carbonate electrolyte at 1 mA cm^{-2} and 1 mAh cm^{-2}. Both the Li-Mg and Li-Ag solid solution anodes exhibited significantly extended cycle life of >240 cycles (480 h) in comparison to <140 cycles (280 h) for pure Li foil electrode. The corresponding voltage hysteresis for these anodes we compared in Figure 3b. The values of voltage hysteresis for the pure Li anode continuously increased from 25 mV for the 1st cycle, to 50 mV for the 100th cycle and 100 mV for the 120th cycle. In contrast, the Li-Mg and Li-Ag solid solution anodes displayed stable voltage hysteresis during cycling. Typically, the value of voltage hysteresis for the Li-Ag solid solution anode remained ≈25 mV for 200 cycles. Figure 3c, d showed voltage-time profiles of the initial and selected cycles (the 1st, 75th, and 100th cycle) for pure Li and Li-Ag solid solution foil electrodes. The overpotential of the pure Li foil electrode showed a significant spike at the initial charge process, indicating its large nucleation barrier, while the Li-Ag electrode exhibited lower overpotential and more smooth voltage curves. The above findings supported that the formation of alloying element-rich interphase could facilitate the electrochemical reaction kinetics and suppress the parasitic reactions between active Li and electrolyte. The Li-Ag foil electrode showed higher current response than the pure Li foil electrode in the cyclic voltammetry (CV) curves, again verifying the fast electrochemical reaction kinetics (Figure S6, Supporting Information). As depicted in Figure S7, Supporting Information, the measured average Coulombic efficiency (ACE) values for Li-Ag and pure Li electrodes were 98.5% and 96.2%, respectively, indicating the significantly improved Li utilization of the thin Li-Ag solid solution electrode. Thus, a long cyclic lifespan of Li metal anodes with high Li utilization can be

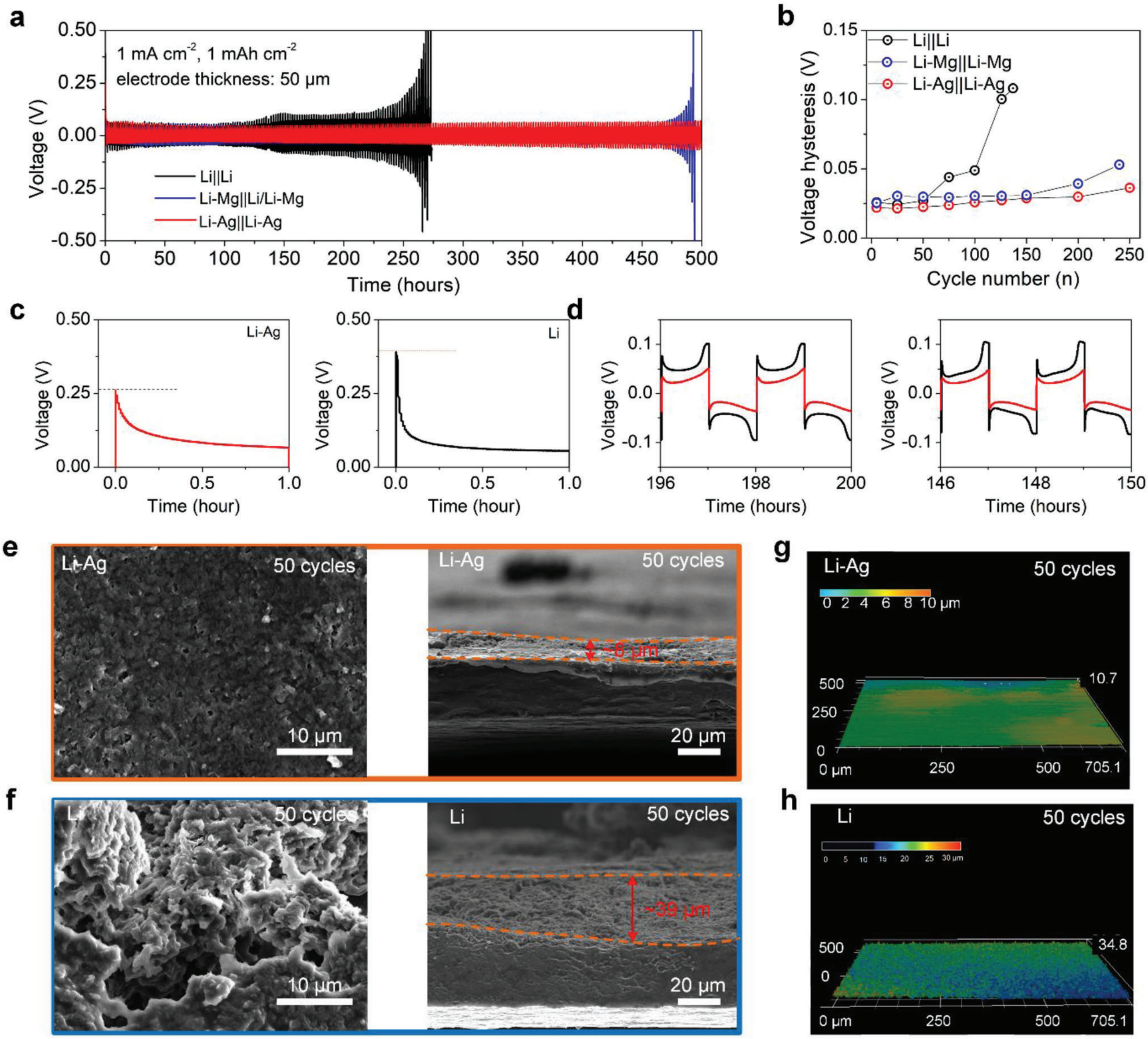

Figure 3. a) Voltage profiles of the Li||Li, Li-Mg||Li-Mg and Li-Ag||Li-Ag cells (electrode thickness of 50 μm and alloying element content of 10 wt%), and b) the corresponding voltage hysteresis at different cycles. c,d) Enlarged charge/discharge curves of the Li||Li and Li-Ag||Li-Ag cells at different cycles. Top-view and cross-section SEM images of e) the Li-Ag and f) pure Li foil electrodes after 50 cycles at 1 mA cm^{-2} and 1 mAh cm^{-2} and g,h) the corresponding LSCM images of the cycled Li-Ag and Li foil electrodes.

expected by the mechanism of dynamic concentration of alloying element at anode interface due to its effect on enhancing reaction kinetics and stability.

We further analyzed the structures and components for the pure Li and Li solid solution electrodes after electrochemical cycles. The scanning electron microscope (SEM) images of Li-Ag foil electrode exhibited a planar surface after 50 cycles (Figure 3e), demonstrating a thin and dense reaction layer with a thickness of ~8 μm. In sharp contrast, the pure Li anode showed a porous, loose electrode structure with a 39 μm-thick reaction layer under the same test condition (Figure 3f). The comparison in roughness for both cycled electrodes was further conducted using laser confocal microscope (LSCM). The results revealed a planar surface for the cycled Li-Ag foil anode (Figure 3g), significantly different from a rough and rugged surface for the pure Li foil anode (Figure 3h).[43] Time-of-flight secondary ion mass spectrometry (TOF-SIMS) method was further conducted on the Li-Ag foil electrode after 50 cycles. The result showed the uniform distribution of the Li and Ag elements on the electrode surface (Figure S8, Supporting Information), indicating that the Ag element could be effective on regulating Li stripping/plating processes over long-term cycling. It is noted that a planar surface was also maintained for the Li-Ag foil electrode after further extending the cycle times (Figure S9, Supporting Information), and the thickness of the reaction layer was only ≈21 μm after 100 cycles, outperforming the pure Li foil electrode with a loose electrode structure and a ~70 µm-thick reaction layer after 100 cycles.[44] The electrochemical impedance spectroscopy (EIS) of the cycled pure Li and Li-Ag foil anodes was also measured after 100 cycles, which demonstrated a lower interface impedance for the Li-Ag foil electrode than the pure Li electrode (Figure S10, Supporting Information). Maintaining thin and dense reaction layer with low interface resistance supported high Li utilization and suppressed side reactions for the Li-Ag electrode.[45,46] Therefore, long cycle life could be expected in practical high energy density rechargeable Li metal batteries with (ultra)thin Li-Ag foil anode based on the mechanism of dynamic concentration of alloying element on anode surface.

The surficial composite of the cycled electrodes was further analyzed. To compare the Ag element content on electrode surface after different cycles, we provided BSE images of Li-Ag foil electrodes after 10, 30, and 50 cycles at the Li stripping state at 1 mA cm^{-2} and 1 mAh cm^{-2} and the corresponding Ag element mapping images (Figure S11, Supporting Information). The results showed that the signals for Ag element remained roughly unchanged for different electrodes. We performed X-ray photoelectron spectroscopy (XPS) measurement on the Li-Ag electrode after 50 cycles at 1 mA cm^{-2} and 1 mAh cm^{-2} (Figure S12, Supporting Information). The high-resolution Ag 3d spectrum exhibited prominent peaks at ≈369.6 and 375.6 eV, suggesting the consistent presence of Ag on electrode surface on cycling and afford the long-term effect for the regulation of Li plating/stripping during cycling. We then applied higher cycling capacity to show the surfacial composite evelutions. Ag element was concentrated on the Li-Ag foil electrode surface after initial electrochemical Li stripping (3 mA cm^{-2} and 3 mAh cm^{-2}). The cells before and after resting (72 hours) were disassembled and the electrodes were investigated by AES spectra (Figure S13, Supporting Information). The surficial atom ratios of Li and Ag before and after resting were 80.1:19.9 and 80.5:19.5, respectively, indicating the good stability of the Ag-rich interface. We then performed BSE imaging and element mapping on the Li-Ag electrode at Li stripping state after 100 cycles at 3 mA cm^{-2} and 3 mAh cm^{-2}. The results showed the clear signal of Ag over the measured area of the electrode (Figure S14, Supporting Information), supporting that the concentrated Ag existed on the electrode surface upon long-term cycling.

2.3. Application in Full Cell and Pouch Cell

The improved Li utilization of the Li solid solution anodes encourages us to explore its practical feasibility toward high energy density rechargeable Li metal batteries with low N/P and E/C ratios. Ultrathin Li-Ag solid solution foil electrodes were further evaluated in full cells paired with two different cathodes (NCM622 and sulfide polyacrylonitrile, SPAN). A high reversible capacity of ≈160 mAh g^{-1} and high capacity retention of ≈95% for 100 cycles were achieved for the NCM622||Li-Ag cell with a 40 µm-thick anode and a low N/P ratio of 2.6. Although the NCM622||Li cell displayed similar initial capacity (~170 mAh g^{-1}) under the same test condition, its capacity quickly decayed after 60 cycles and the capacity retention was only ~80% for 70 cycles (**Figure 4**a,b). The corresponding voltage curves for the 1st and 50th cycle are shown in Figure 4c,d. The NCM622||Li cell demonstrated a "bump" shape curve during the initial charge process in comparison to smooth curve for that of the NCM622||Li-Ag cell, indicating the decreased Li nucleation barrier after introducing alloying element Ag (Figure 4c).[47,48] Besides, the NCM622||Li-Ag cell displayed reduced voltage hysteresis in the charge and discharge curves for the 50th cycle in comparison to that of the NCM622||Li cell, which indicated the employment of Li-Ag anode could reduce cell polarization and enhance electrochemical stability (Figure 4d). Postanalysis of the anodes was further conducted to reveal the origins of the improved cell performance for NCM622||Li-Ag cell. Although cathodes from both cells exhibited well-maintained structure after 100 cycles (Figure S15, Supporting Information), Li-Ag anode exhibited a planar surface and good structural integrity after 100 cycles, in sharp comparison with porous and rugged morphology of the cycled Li anode (Figure 4e,f), revealing that the dynamic concentration of alloying element on anode surface significantly facilitated electrochemical stability of full batteries. To further show the advantages of our dynamic concentration of alloying element on anode surface in prolonging the battery cycle life, full cells with high-areal-capacity SPAN cathode (≈3.3 mAh cm^{-2}) and ultrathin Li-Ag anode (40 µm) were assembled, which delivered stable cycling performance with a high capacity retention of 98% for 80 cycles, far outperforming the counterpart with pure Li anode (Figure 4g).

To demonstrate the effect of the dynamic concentration of alloying element at Li solid solution interface, we investigated the Li nucleation overpotential with different initial Ag concentrations on electrode surface. After electrochemically stripping of different amounts of active Li (3 mAh cm^{-2}, 5 mAh cm^{-2}, and 7 mAh cm^{-2}), Li-A electrodes with different alloying element A concentrations were produced and electrochemical Li plating was then conducted on these anodes at 1 mA cm^{-2}. According to the recorded potential curves, different Li nucleation overpotentials were shown for Li-A electrodes after different amounts of active Li stripping (0, 3, 5, and 7 mAh cm^{-2}) (Figure 4h). The nucleation overpotential for the initial Li-Ag electrode was ≈86 mV, it was reduced to ≈73 mV for that after 3 mAh cm^{-2} of Li stripping capacity, and further reduced to ≈54 and ≈56 mV for that after Li stripping for 5 and 7 mAh cm^{-2}, respectively (Figure 4i). We further conducted a comprehensive comparison on the Ag element contents of Li-Ag foil electrodes after stripping different amounts of Li by the results of EPMA and AES tests (Figures S16 and S17, Supporting Information). The EPMA results showed a significant increase in the surficial Ag concentration for the sample after stripping 3 mAh cm^{-2} of Li in comparison to the sample after stripping 5 mAh cm^{-2} of Li, and then slight increased for the sample after stripping 7 mAh cm^{-2} of Li. The AES results provided atom ratios of Li:Ag for the electrodes after stripping 3, 5, and 7 mAh cm^{-2} of Li as 81.1:19.9, 45:55, and 43:57, respectively, which were consistent with the EPMA results. These results explained why the Li nucleation overpotential did not vary on the anode after stripping 5 and 7 mAh cm^{-2} of Li. Furthermore, we conducted additional electrochemical Li deposition tests on pure Ag foil electrode with a thickness of 1 µm, and the Li nucleation overpotential was recorded as 47 mV (Figure S18, Supporting Information), which was lower than that for Li-Ag foil anode with different surficial Ag contents (Figure 4i). This finding is consistent with our initial explanation that the Li nucleation barrier

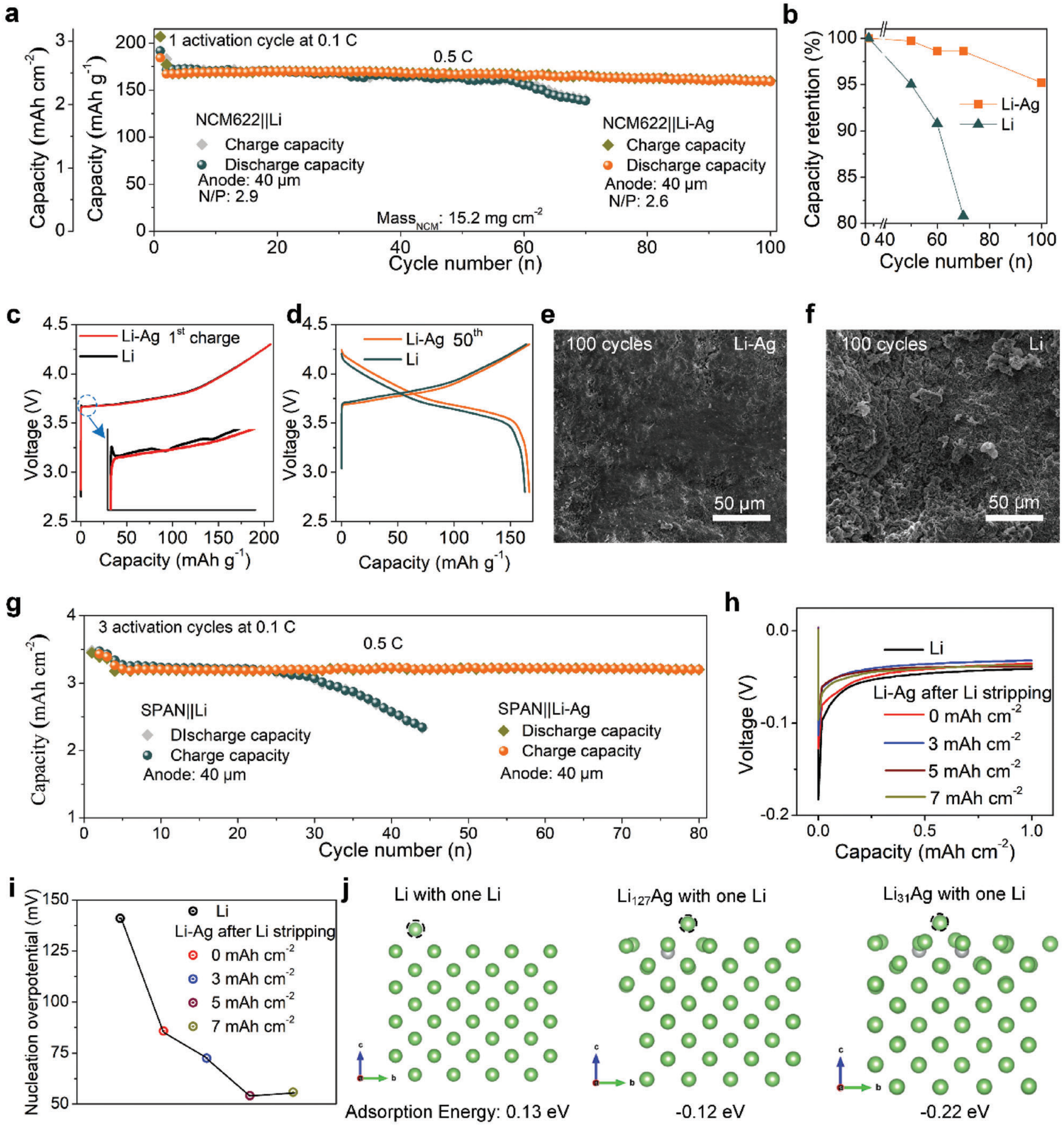

Figure 4. a) Capacity-cycle number plots of the NCM622||Li and NCM622||Li-Ag cells with anode thickness of 40 µm and cathode mass loading of 15.2 mg cm^{-2}, b) the corresponding capacity retention for selected cycles, c) the 1st cycle charge profile and d) the voltage-capacity curves for the 50th cycle. e,f) SEM images of the Li-Ag and pure Li foil electrodes after 100 cycles. g) Capacity-cycle number plots of the SPAN||Li and SPAN||Li-Ag cells with cathode areal capacity of ≈3.3 mAh cm^{-2} and anode thickness of 40 µm. h,i) Nucleation overpotential curves for the Li deposition on Li-Ag electrode after different amounts of active Li stripping (0, 3, 5, and 7 mAh cm^{-2}). The current density for Li plating was 1 mA cm^{-2}. j) The atomic structures of Li-ion adsorption on the Li (100), Li$_{127}$Ag (100), and Li$_{31}$Ag (100) surfaces.

decreases with an increase in Ag concentration. These Li-Ag electrodes showed planar Li deposition (Figures S19 and S20, Supporting Information), while the pure Li electrode exhibited disordered Li dendrite deposits with loose structure. Besides, similar phenomenon was observed for Li-Mg electrode (Figure S21, Supporting Information).

Density function theory (DFT) calculation of the adsorption energy between Li and Li-Ag with different Ag contents were

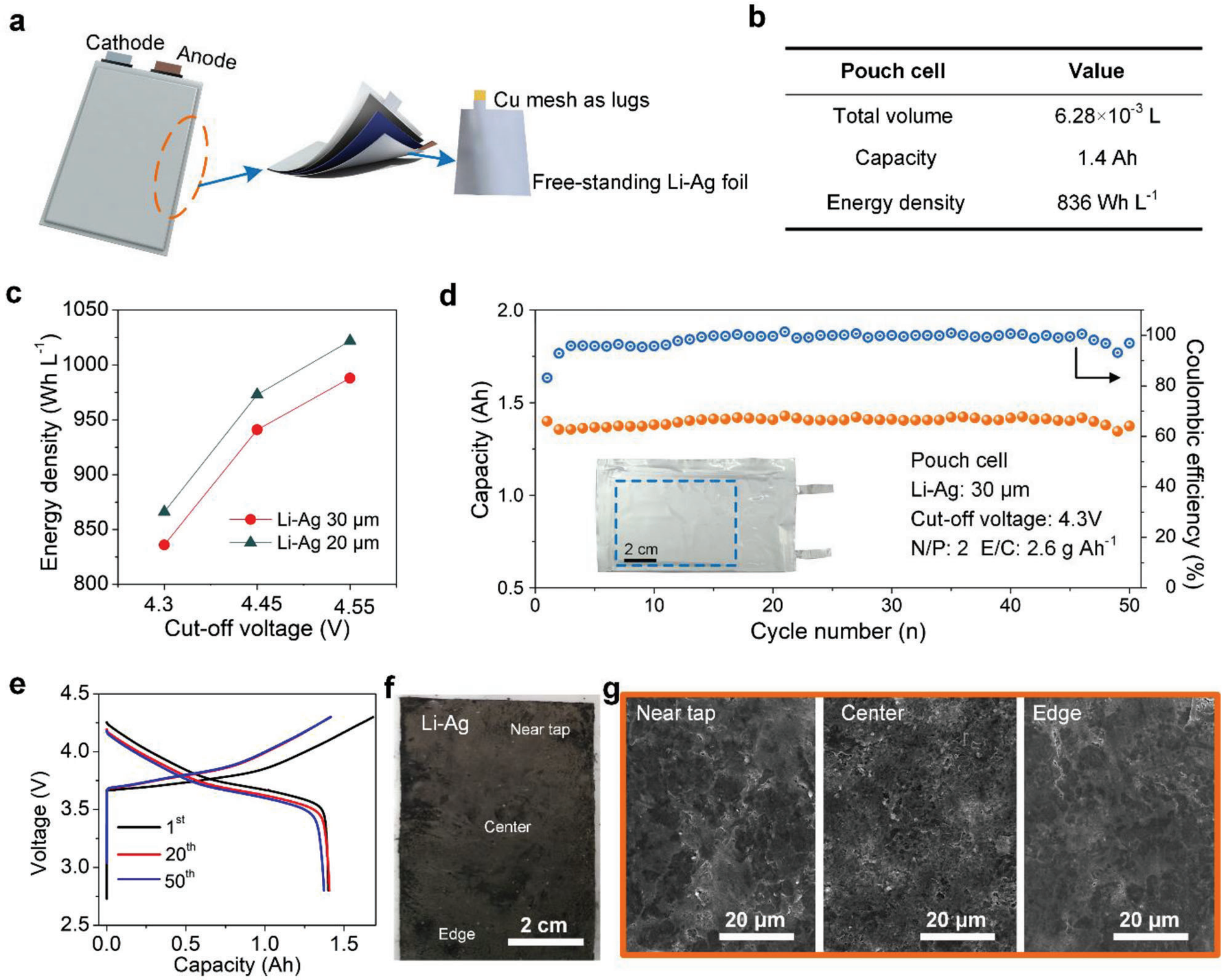

Pouch cell	Value
Total volume	6.28×10^{-3} L
Capacity	1.4 Ah
Energy density	836 Wh L^{-1}

Figure 5. a) Schematic of the Ah-level laminated pouch cell and b) details for the capacity and energy density of as-assembled cell. c) The calculated energy density of the pouch cell with different cut-off voltages and anode thicknesses. d) Electrochemical cycling of the laminated pouch cell employing 30 µm-thick Li-Ag foil anode and NCM622 cathode with a N/P ratio of 2 and a E/C ratio of 2.6 Ah^{-1}, and e) the corresponding voltage-capacity curves for the 1st, 20th and 50th cycle. f) Digital image of the cycled Li-Ag foil electrode in the pouch cell, and g) the corresponding SEM images at different regions.

further conducted to further explain the effect of alloying element enriched electrode surface on regulating the Li plating/stripping property. In our study, a Li-Ag solid solution with a mass ratio of 10 wt% Ag and 90 wt% Li (an atom ratio of Li to Ag of ≈127:1) was used as typical example for demonstration. To support the as-proposed mechanism, we calculated and compared the Li ion adsorption energies on (100) face for Li-Ag electrodes with different Ag content surfaces (pure Li, $Li_{127}Ag$ with Li/Ag atomic ratio of 127 and mass ratio of 90/10, and $Li_{31}Ag$ with Li/Ag atomic ratio of 31 and mass ratio of 70/30). The calculated values were 0.13, −0.12, and −0.22 eV, respectively (Figure 4j), which indicated that the Li nucleation barrier decreased as the Ag content increased. However, a high mass ratio of Ag could result in a low capacity (≈2700 mAh g^{-1}, for Li-Ag foil electrode with 30 wt% Ag and 70 wt% Li). To address this issue, we initially introduced 10 wt% Ag to pursuit a high anode capacity. We observed that the surficial Ag concentration increased with Li stripping, thereby ensuring long-term cycling stability that Li composites with high-content intermetallic compounds could endure. The dynamical formation of the higher Ag concentration on the electrode surface could further regulate the Li plating processes, ensuring its validity for electrochemical cycling under high Li utilization and achieving high energy density of batteries.

The Li-Ag foil exhibited excellent processability. We fabricated an ultrathin Li-Ag foil with a size of 50 × 4 cm and a thickness of 25 µm, which demonstrated the operation capability for folding, rolling, and restoring to its original state (Figure S22a, Supporting Information). Additionally, we produced foils with controllable thicknesses ranging from 25 to 5 µm (Figure S22b, Supporting Information), which enabled the anode to be used in high-energy-density batteries. To further reveal the advances of interfacial dynamical alloying element concentration in enabling high energy density batteries, Ah-level laminated pouch cells were assembled using ultrathin Li-Ag solid solution foil anode (30 µm) with low N/P ratio (2) and low E/C ratio (2.6 g Ah^{-1}) (**Figure 5**a). The parameter of the pouch cell was shown in Table S2, Supporting Information. With a reversible capacity of ∼1.4 Ah at 0.2 *C* (1 *C* = 1.4 A), the cell demonstrated a high energy density of 836 Wh L^{-1} based on the total volume of the cell (Figure 5b). The higher energy density of batteries can be achieved by increasing the cut-off charge voltage (Figures S23–S25, Supporting Information). For example, by increasing the cutoff voltage from 4.3 to 4.55 V, the discharge capacity and mid-value voltage increased from 184.3 to 211.4 mAh g^{-1} and 3.77 to 3.81 V, respectively, delivering a 16% increase in energy density. Also, the employment of an anode with thinner thickness further reduced the cell volume and increased the energy density (Figure 5c and S26, Supporting Information). Impressively, the 1.4 Ah-laminated pouch cell delivered stable charge/discharge cycling performance with a high capacity retention of 95.5% after 50 cycles (Figure 5d) and demonstrated well-overlapped voltage-capacity curves with only slight increase in voltage polarization on cycling (10 mV from 20 to 50 cycles) (Figure 5e), demonstrating the great potential in achieving high energy density batteries with long lifespan. Smooth and dense surface over different test regions of the Li-Ag foil electrode was shown for the cycled ultrathin Li-Ag foil anode, including near tap, the central, and the edge regions (Figure 5f,g). Such results confirmed that uniform, planar Li plating/stripping was successfully realized over the entire Li-Ag foil anode in pouch cell configuration, which suggested the practical implantation of the ultrathin Li-Ag foil anode in high energy density batteries. To achieve high energy density, $LiNi_{0.8}Co_{0.1}Mn_{0.1}O_2$ (NCM811) cathode with a high mass loading of ≈21 mg cm^{-2} was used as the cathode to pair 30 μm-thick Li-Ag foil anode to assemble laminated pouch cell. The cell delivered a total capacity of 5.2 Ah and a high energy density of 483 Wh kg^{-1} (Figure S27, Supporting Information).

3. Conclusion

In summary, a dynamic concentration of alloying element at anode interface was revealed for Li solid solution foil electrodes upon Li stripping/plating cycling, which enabled a low nucleation barrier with dense and planar Li deposition and superior cycle life. Alloying element-rich interface would be formed during the Li stripping processes, which enabled reduced Li nucleation barrier and regulated the subsequent Li deposition with dense and planar surface. The formation of inactive Li was significantly suppressed, and the cycling lifespan was greatly improved. The practical feasibility of the Li solid solution anode was evidenced by its application in Ah-level laminated pouch cell under harsh conditions. With an ultrathin Li-Ag solid solution anode (30 μm), 1.4 Ah laminated pouch cell demonstrated a high energy density of 836 Wh L^{-1} and stable electrochemical cycling performance with a low N/P ratio (2) and E/C ratio (2.6 g Ah^{-1}). The mechanism of dynamic concentration of alloying element at electrode interface revealed in this work provides new sights into advanced Li metal anode design toward practical high energy density rechargeable batteries.

4. Experimental Section

Materials Preparation: Li-Ag, Li-Mg, and Li-Ag/LiCl foils were synthesized utilizing the reaction between the molten Li and the corresponding Ag, Mg, and AgCl at a temperature of 250 °C, respectively. The weight ratio of the metal Ag, Mg, or AgCl to Li was 1:9. The as-prepared molten composites were cooled down to room temperature and then calendared to certain thickness using a roll squeezer. The pure Li was molten, cooled, and calendared to prepare the pure Li electrode, accordingly. The above processes were conducted in Ar-filled glove box.

The SPAN cathode with active mass loading of ≈5 mg cm^{-2} was prepared using a slurry process, which consisted of 85 wt% SPAN, 7.5 wt% carbon black, and 7.5 wt% lithium polyacrylate acid (LiPAA) binder. NCM622 cathode with active material mass loading of ≈15.2 mg cm^{-2} was fabricated with the same procedure. The mass ratio of active material, carbon black, and poly(vinylidenefluoride) (PVDF) in the NCM622 cathode was 92:4:4. NCM811 cathode with active material mass loading of ≈21 mg cm^{-2} was fabricated through the same way. The mass ratio of active material, carbon black, and PVDF in the NCM622 cathode was 98:1:1.

Materials Characterization: The morphologies of the samples were characterized by SEM (Nova NanoSEM 450). BSE images and the corresponding elemental mapping images were collected by EPMA (8050G). The composition information over different sample depths was detected by AES (JAMP-9510F) and TOF-SIMS (IONTOF GmbH, Germany measurements) with the Ar$^+$ etching method. X-ray photoelectron spectroscopy (XPS, AXIS-ULTRA DLD-600 W) was performed to analyze the surfacial composite. The LSCM images were collected by the Keyence VK-X200K microscope.

Electrochemical Test: 2032-type coin cell was used to evaluate the electrochemical performance. 1 M $LiPF_6$ in ethylene carbonate (EC)/dimethyl carbonate (DEC) (1:1 in volume) with 5 wt% fluoroethylene carbonate (FEC) was used as electrolyte. CV for symmetric cells was performed in the voltage range from −0.1 to 0.1 V (vs Li/Li$^+$) at the scan rate of 0.1 mV s^{-1}. EIS was tested in the frequency range between 100 mHz and 100 kHz in an open-circuit state. VMP3 electrochemical workstation (Bio-Logic) was used for the CV and EIS tests. SPAN-based full cells were activated at 0.1 *C* (1 *C* = 700 mA g^{-1}) for three activation cycles and then cycled at 0.5 *C* with the voltage ranging from 1 to 3 V (vs Li/Li$^+$). NCM622-based full cells were activated at 0.1 *C* (1 *C* = 175 mA g^{-1}) and cycled at 0.5 *C* from 4.3 V to 2.8 V (vs Li/Li$^+$). Ah-level laminated Li-Ag||NCM622 pouch cell was activated at 0.1 *C* and cycled at 0.2 *C*, and the energy density was calculated based on the medium voltage of initial discharging process and the total volume of the pouch cell.

Density Function Theory (DFT) Calculation: The Li-ion adsorption energies on the Li (100), $Li_{127}Ag$ (100), $Li_{31}Ag$ (100), and $Li_{15}Ag$ (100) surfaces were calculated (The atom ratios for Li-Ag were defined according to the mass ratio of Li/Ag in 90:10, and 70:30). After the relaxation of slab structures, five different adsorption sites were checked and the site with the lowest energy was selected for adsorption energy calculation. The adsorption energy E_{ad} was described as follows[49]:

$$E_{ad}=E_{slab+Li}-(E_{slab}+E_{Li}) \tag{1}$$

Where d is the total energy of the slab structure bonding with one Li, E_{sub} is the total energy of the surface structure, and E_{Li} is the total energy of one Li.

Supporting Information

Supporting Information is available from the Wiley Online Library or from the author.

Acknowledgements

The authors would like to thank the support by the National Natural Science Foundation of China (No. 52272207 and No. 52072137). Y.H. would like to thank the support by China Postdoctoral Science Foundation (No. 2022M711791). Z.C. gratefully acknowledged financial support from the National Natural Science Foundation of China (No. 22205068). The authors would like to thank the Analytical and Testing Center of Huazhong

University of Science and Technology for conducting the materials characterization. The authors would like to thank the Analytical and Testing Center of Huazhong University of Science and Technology for conducting the materials characterization. The authors would like to acknowleged X.G. in School of Materials Science and Engineering, Huazhong University of Science and Technology for the AES tests.

Conflict of Interest

The authors declare no conflict of interest.

Data Availability Statement

The data that support the findings of this study are available from the corresponding author upon reasonable request.

Keywords

anode interfaces, dynamic concentration of alloying elements, Li metal batteries, Li solid solution anodes

Received: June 27, 2023
Revised: August 20, 2023
Published online:

---

[1] D. Lin, Y. Liu, Y. Cui, *Nat. Nanotechnol.* **2017**, *12*, 194.
[2] J. Liu, Z. Bao, Y. Cui, E. J. Dufek, J. B. Goodenough, P. Khalifah, Q. Li, B. Y. Liaw, P. Liu, A. Manthiram, Y. S. Meng, V. R. Subramanian, M. F. Toney, V. V. Viswanathan, M. S. Whittingham, J. Xiao, W. Xu, J. Yang, X.-Q. Yang, J.-G. Zhang, *Nat. Energy* **2019**, *4*, 180.
[3] M. Li, J. Lu, Z. Chen, K. Amine, *Adv. Mater.* **2018**, *30*, 1800561.
[4] T. Ma, Y. Ni, Q. Wang, W. Zhang, S. Jin, S. Zheng, X. Yang, Y. Hou, Z. Tao, J. Chen, *Angew. Chem., Int. Ed.* **2022**, *61*, 202207927.
[5] W. Wu, W. Luo, Y. Huang, *Chem. Soc. Rev.* **2023**, *52*, 2553.
[6] R. Weber, M. Genovese, A. J. Louli, S. Hames, C. Martin, I. G. Hill, J. R. Dahn, *Nat. Energy* **2019**, *4*, 683.
[7] L. Dong, S. Zhong, B. Yuan, Y. Li, J. Liu, Y. Ji, D. Chen, Y. Liu, C. Yang, J. Han, W. He, *Angew. Chem., Int. Ed.* **2023**, *62*, 202301073.
[8] Y. Zhang, P. Zhao, Q. Nie, Y. Li, R. Guo, Y. Hong, J. Deng, J. Song, *Adv. Mater.* **2023**, *35*, 2211032.
[9] M. S. Kim, Z. Zhang, P. E. Rudnicki, Z. Yu, J. Wang, H. Wang, S. T. Oyakhire, Y. Chen, S. C. Kim, W. Zhang, D. T. Boyle, X. Kong, R. Xu, Z. Huang, W. Huang, S. F. Bent, L.-W. Wang, J. Qin, Z. Bao, Y. Cui, *Nat. Mater.* **2022**, *21*, 445.
[10] H. Zhang, Z. Zeng, F. Ma, Q. Wu, X. Wang, S. Cheng, J. Xie, *Angew. Chem., Int. Ed.* **2023**, *62*, 202300771.
[11] C. Luo, H. Hu, T. Zhang, S. Wen, R. Wang, Y. An, S. S. Chi, J. Wang, C. Wang, J. Chang, Z. Zheng, Y. Deng, *Adv. Mater.* **2022**, *34*, 2205677.
[12] X. Cao, X. Ren, L. Zou, M. H. Engelhard, W. Huang, H. Wang, B. E. Matthews, H. Lee, C. Niu, B. W. Arey, Y. Cui, C. Wang, J. Xiao, J. Liu, W. Xu, J.-G. Zhang, *Nat. Energy* **2019**, *4*, 796.
[13] S. Kim, T. K. Lee, S. K. Kwak, N.-S. Choi, *ACS Energy Lett.* **2021**, *7*, 67.
[14] M. S. Kim, Z. Zhang, J. Wang, S. T. Oyakhire, S. C. Kim, Z. Yu, Y. Chen, D. T. Boyle, Y. Ye, Z. Huang, W. Zhang, R. Xu, P. Sayavong, S. F. Bent, J. Qin, Z. Bao, Y. Cui, *ACS Nano* **2023**, *17*, 3168.
[15] X. Jin, Z. Cai, X. Zhang, J. Yu, Q. He, Z. Lu, M. Dahbi, J. Alami, J. Lu, K. Amine, H. Zhang, *Adv. Mater.* **2022**, *34*, 2200181.
[16] A. Hu, W. Chen, X. Du, Y. Hu, T. Lei, H. Wang, L. Xue, Y. Li, H. Sun, Y. Yan, J. Long, C. Shu, J. Zhu, B. Li, X. Wang, J. Xiong, *Energy Environ. Sci.* **2021**, *14*, 4115.
[17] Z. Huang, J.-C. Lai, S.-L. Liao, Z. Yu, Y. Chen, W. Yu, H. Gong, X. Gao, Y. Yang, J. Qin, Y. Cui, Z. Bao, *Nat. Energy* **2023**, *8*, 577.
[18] Y. Wang, Z. Qu, S. Geng, M. Liao, L. Ye, Z. Shadike, X. Zhao, S. Wang, Q. Xu, B. Yuan, X. Zhang, X. Gao, X. Jiang, H. Peng, H. Sun, *Angew. Chem., Int. Ed.* **2023**, *62*, 202304978.
[19] M. Zhang, K. Liu, Y. Gan, H. Wang, F. Liu, M. Bai, X. Tang, Z. Wang, S. Li, A. Shao, K. Zhou, T. Wang, Z. Wang, S. Yuan, Y. Ma, *Adv. Energy Mater.* **2022**, *12*, 2201390.
[20] H. Chen, Z. Cao, J. Gu, Y. Cui, Y. Zhang, Z. Zhao, Z. Cheng, Q. Zhao, B. Li, S. Yang, *Adv. Energy Mater.* **2021**, *11*, 2003746.
[21] C.-Y. Wang, Z.-J. Zheng, Y.-Q. Feng, H. Ye, F.-F. Cao, Z.-P. Guo, *Nano Energy* **2020**, *74*, 104817.
[22] Y. Li, J. Li, H. Xiao, T. Xie, W. Zheng, J. He, H. Zhu, S. Huang, *Adv. Funct. Mater.* **2023**, *33*, 2213905.
[23] Y. He, M. Zhang, A. Wang, B. Zhang, H. Pham, Q. Hu, L. Sheng, H. Xu, L. Wang, J. Park, X. He, *ACS Appl. Mater. Interfaces* **2022**, *14*, 33952.
[24] J. M. Wrogemann, M. J. Luther, P. Barmann, M. Lounasvuori, A. Javed, M. Tiemann, R. Golnak, J. Xiao, T. Petit, T. Placke, M. Winter, *Angew. Chem., Int. Ed.* **2023**, *62*, 202303111.
[25] J. B. Park, C. Choi, S. Yu, K. Y. Chung, D. W. Kim, *Adv. Energy Mater.* **2021**, *11*, 2101544.
[26] M. Wan, S. Kang, L. Wang, H. W. Lee, G. W. Zheng, Y. Cui, Y. Sun, *Nat. Commun.* **2020**, *11*, 829.
[27] S. Liu, Y. Ma, Z. Zhou, S. Lou, H. Huo, P. Zuo, J. Wang, C. Du, G. Yin, Y. Gao, *Energy Storage Mater.* **2020**, *33*, 423.
[28] Z. Wang, T. Chen, Y. Liu, J. Xing, A. Zhou, J. Li, W. Zou, F. Zhou, *Chem. Eng. J.* **2022**, *430*, 132970.
[29] S. Jin, Y. Ye, Y. Niu, Y. Xu, H. Jin, J. Wang, Z. Sun, A. Cao, X. Wu, Y. Luo, H. Ji, L. J. Wan, *J. Am. Chem. Soc.* **2020**, *142*, 8818.
[30] P. Shi, L. P. Hou, C. B. Jin, Y. Xiao, Y. X. Yao, J. Xie, B. Q. Li, X. Q. Zhang, Q. Zhang, *J. Am. Chem. Soc.* **2022**, *144*, 212.
[31] W. Jia, Y. Liu, Z. Wang, F. Qing, J. Li, Y. Wang, R. Xiao, A. Zhou, G. Li, X. Yu, Y. S. Hu, H. Li, Z. Wang, X. Huang, L. Chen, *Sci. Bull.* **2020**, *65*, 1907.
[32] J. Gao, C. Chen, Q. Dong, J. Dai, Y. Yao, T. Li, A. Rundlett, R. Wang, C. Wang, L. Hu, *Adv. Mater.* **2021**, *33*, 2005305.
[33] Y.-G. Lee, S. Fujiki, C. Jung, N. Suzuki, N. Yashiro, R. Omoda, D.-S. Ko, T. Shiratsuchi, T. Sugimoto, S. Ryu, J. H. Ku, T. Watanabe, Y. Park, Y. Aihara, D. Im, I. T. Han, *Nat. Energy* **2020**, *5*, 299.
[34] S. Zhang, G. Yang, Z. Liu, S. Weng, X. Li, X. Wang, Y. Gao, Z. Wang, L. Chen, *ACS Energy Lett.* **2021**, *6*, 4118.
[35] M. Zhu, X. Zhao, R. Yan, J. Zhang, *Curr. Opin. Solid State Mater. Sci.* **2023**, *27*, 101079.
[36] X. Wu, W. Zhang, N. Wu, S. S. Pang, Y. Ding, G. He, *Adv. Energy Mater.* **2021**, *11*, 2003082.
[37] X. Liang, Q. Pang, I. R. Kochetkov, M. S. Sempere, H. Huang, X. Sun, L. F. Nazar, *Nat. Energy* **2017**, *2*, 17119.
[38] G. Li, X. Duan, X. Liu, R. Zhan, X. Wang, J. Du, Z. Chen, Y. Li, Z. Cai, Y. Shen, Y. Sun, *Adv. Mater.* **2023**, *35*, 2207310.
[39] Z. Peng, J. Song, L. Huai, H. Jia, B. Xiao, L. Zou, G. Zhu, A. Martinez, S. Roy, V. Murugesan, H. Lee, X. Ren, Q. Li, B. Liu, X. Li, D. Wang, W. Xu, J. G. Zhang, *Adv. Energy Mater.* **2019**, *9*, 1901764.
[40] Y. Li, G. Yang, C. Zhang, W. Y. Lieu, C. Y. J. Lim, S. Sun, J. Wang, S. Jiang, Z. Xing, Z. Sofer, M. F. Ng, W. Liu, Z. W. Seh, *Adv. Funct. Mater.* **2022**, *33*, 2210639.
[41] H. Kwon, J. H. Lee, Y. Roh, J. Baek, D. J. Shin, J. K. Yoon, H. J. Ha, J. Y. Kim, H. T. Kim, *Nat. Commun.* **2021**, *12*, 5537.
[42] Y. X. Zhan, P. Shi, X. X. Ma, C. B. Jin, Q. K. Zhang, S. J. Yang, B. Q. Li, X. Q. Zhang, J. Q. Huang, *Adv. Energy Mater.* **2021**, *12*, 2103291.
[43] M. Hu, Z. Tong, C. Cui, T. Zhai, H. Li, *Nano Lett.* **2022**, *22*, 3047.
[44] H. Liang, L. Wang, Y. Song, D. Ren, A. Wang, Y. Yang, H. Xu, Y. Sun, X. He, *Adv. Funct. Mater.* **2023**, 2203077. https://doi.org/10.1002/adfm.202303077.

[45] C. Fang, J. Li, M. Zhang, Y. Zhang, F. Yang, J. Z. Lee, M. H. Lee, J. Alvarado, M. A. Schroeder, Y. Yang, B. Lu, N. Williams, M. Ceja, L. Yang, M. Cai, J. Gu, K. Xu, X. Wang, Y. S. Meng, *Nature* **2019**, *572*, 511.

[46] C. Jin, T. Liu, O. Sheng, M. Li, T. Liu, Y. Yuan, J. Nai, Z. Ju, W. Zhang, Y. Liu, Y. Wang, Z. Lin, J. Lu, X. Tao, *Nat. Energy* **2021**, *6*, 378.

[47] D. Lin, Y. Liu, Z. Liang, H. W. Lee, J. Sun, H. Wang, K. Yan, J. Xie, Y. Cui, *Nat. Nanotechnol.* **2016**, *11*, 626.

[48] J. Betz, J. P. Brinkmann, R. Nölle, C. Lürenbaum, M. Kolek, M. C. Stan, M. Winter, T. Placke, *Adv. Energy Mater.* **2019**, *9*, 1900574.

[49] X. Wang, Y. He, S. Tu, L. Fu, Z. Chen, S. Liu, Z. Cai, L. Wang, X. He, Y. Sun, *Energy Storage Mater.* **2022**, *49*, 135.